The present investigation envisages the preparation of a low-density $(Fe_{40}Al_{15}Si_{10}C_1)_{66}(Mn_{19}Ni_{15})_{34}$ high entropy steel by mechanical alloying (MA) and spark plasma sintering (SPS) forming a dual-phase structure of BCC and B2 that may have excellent strength with good amount of ductility. The alloying behaviour, thermal stability, microstructural, and mechanical properties (i.e., microhardness, elastic constant, and compressive strength) during MA and SPS were studied systematically. The mechanical properties of this high entropy steel were also understood with the help of various strengthening mechanisms. Further, wear and biocompatibility of the SPSed samples were examined systematically.

3.1 Prediction of the melting point

The melting point of the high entropy steel was calculated using the machine learning (ML) approach [229], rule of mixture, and CALPHAD, and its values were found to be 1365 ℃ (1638 K), 1347 ℃ (1620 K), and 1210 ℃ (1483 K), respectively. The equations used to calculate the melting point through machine learning approach and rule of mixture are taken from equation 2.7 and 2.8, respectively. The binary solidus temperature $T_{i\text{-}j}$ are displayed in Figure 3.1 (pentagon shape), and T_i is the melting point of the individual elements, and its values are given in Table 2.3. It was ascertained that the prediction of the melting point in the HEAs system through the ML approach was more accurate or precise as compared to the rule of mixture and CALPHAD modelling [229].

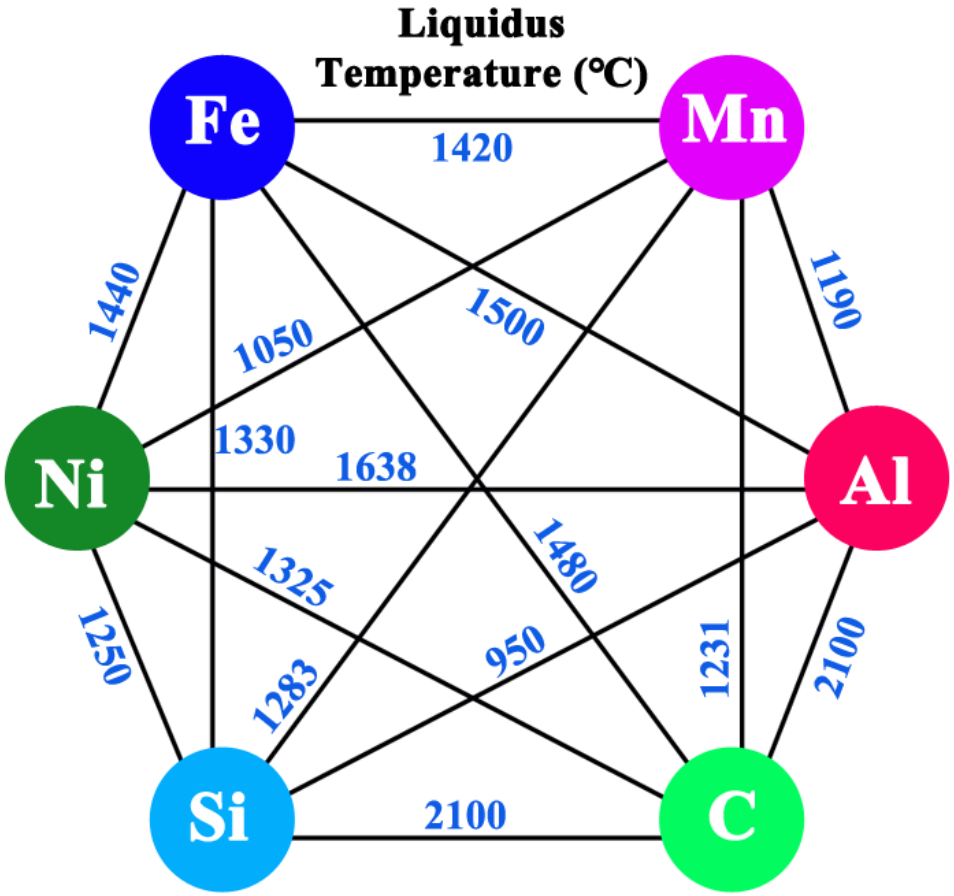

Figure 3.1: Liquidus temperature (°C) values of possible binary compositions in the non-equiatomic FeMnNiAlSiC high entropy steel.

3.2 Alloying behaviour of the $Fe_{40}Mn_{19}Ni_{15}Al_{15}Si_{10}C_1$ HES

Phase evolution study of the milled samples was studied using the XRD analysis at the interval of 5 h, which is illustrated in Figure 3.2(a). The pre-mixed powders of alloying elements reveal the diffraction peaks related to the pure elements i.e., Fe (cI2, JCPDS# 00-006-0696), α-Mn (cI58, JCPDS# 00-032-0637), Ni (cF4, JCPDS# 00-004-0850), Al (cF4, JCPDS# 00-004-0787), Si (cF8, JCPDS# 00-005-0565), and C (hP4, JCPDS# 00-056-0159). It is evident (from Figure 3.2(a)) that the diffraction peak intensity of all the elements decreases with the milling time. Low intensity peaks of all the elements vanish under 5 h of milling. Al vanishes under 15 h of milling, which indicates that Al has the highest alloying rate in the alloy. After 20 h, intense

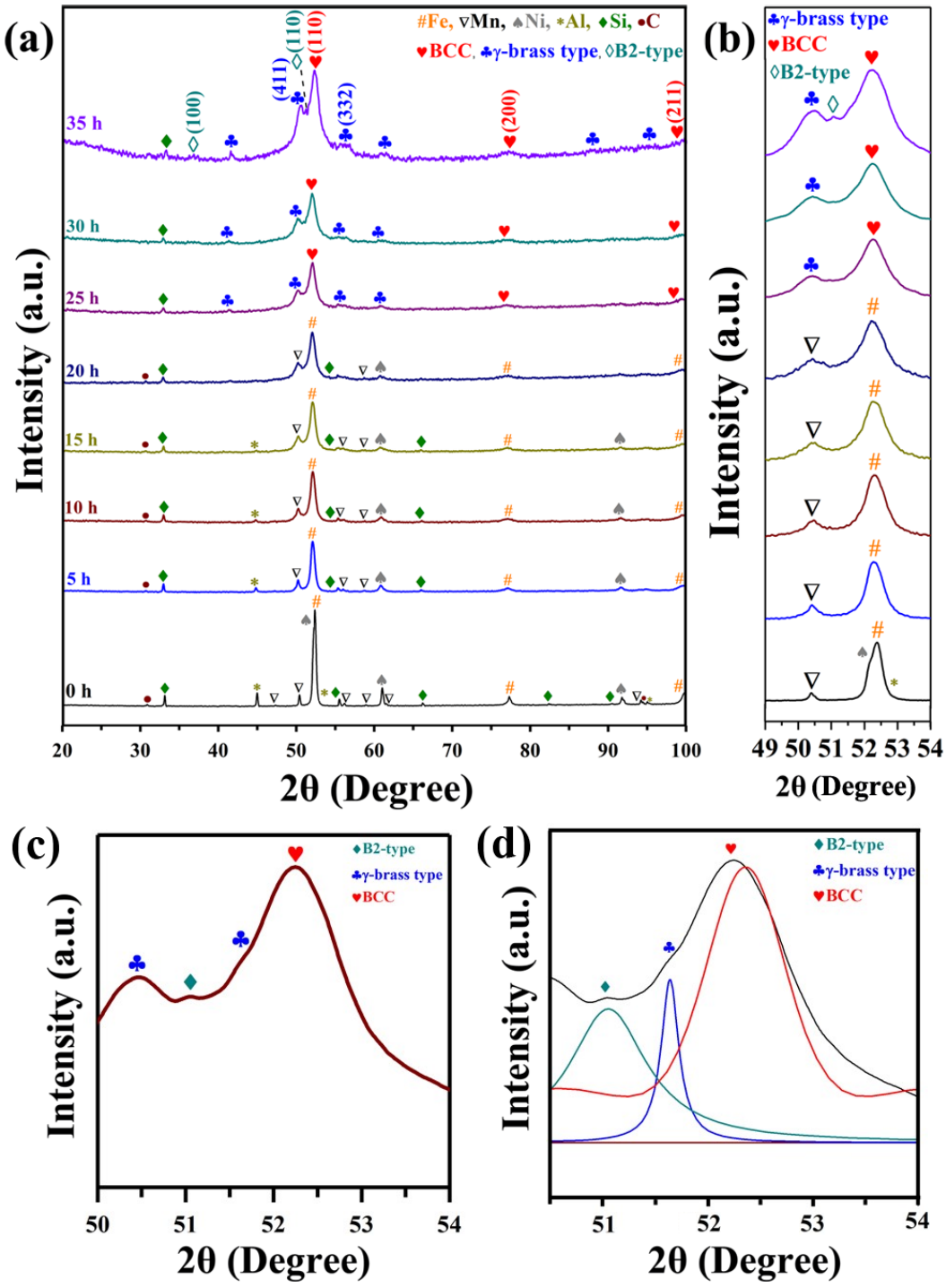

Figure 3.2: (a) XRD patterns of the milled samples at various milling time; (b) Enlarged view along the (110) plane in 2θ range from 49º- 54º; (c) Blown-up image along the (110) plane; (d) Deconvulated image in between 2θ range from 50.5º- 54º. This shows the alloying behaviour of elements with milling time and finally formed the multi-phase structure (BCC, γ-brass type and B2-type) coexisted with trace amount of Si.

peaks of Ni and Mn were not evident in the diffraction pattern. The alloying behaviour of the elements with milling time is related to the diffusion of low melting point elements into the matrix of higher melting point elements, as reported previously [230,231]. The solid solution was formed under 25 h of milling, which is evident in Figure 3.2(a). The phases formed are BCC (a = 0.286 nm; JCPDS# 00-006-0696) and γ-brass type (a = 0.882 nm; JCPDS# 01-078-2831) structure. Figure 3.2(b) illustrates the XRD pattern with the milling time along the (110) plane in the 2θ range from 49º- 54º. The milling was extended up to 35 h, for further nanostructuring of milled powder and formation of homogenous solid solution. However, the new phase B2-type structure was formed. Minor peak broadening and the decrease in the amount of Si occurred as milling extended to 35 h. The Figure 3.2 (c and d) shows the blown-up image and the deconvoluted image along the (110) plane to have better clarity of three phase peaks. It is evident from Figure 3.3 (a) that the trace amount of Si remained even after 35 h of milling. After the milling, the BCC as a major phase, γ-brass type, and B2-type (a = 0.290 nm, JCPDS# 01-083-3994) coexisted with the undissolved Si, as illustrated in Figure 3.3(a). The milled powder sample after the milling did not show any kind of contamination, which is confirmed through X-ray energy dispersive spectroscopy and X-ray diffraction (Figure 3.2(a)). In our previous investigation on the Al matrix composites and quasicrystals milled for more than 50 h in WC vials and with WC balls, no signature of contamination was detected [112, 232]. Figure 3.3(b) displays the Rietveld refinement of a 35 h milled powder sample. This also ascertained that the 35 h milled powder sample formed the multi-phase structure i.e., BCC, B2-type, and γ-brass type along with the presence of undissolved Si. The crystallite size and lattice strain of the milled samples were calculated using the Rietveld refinement method with the help of GSAS-II, as listed in Table 3.1. The crystallite size was found to decrease with the milling time, which is evident from Table 3.1.

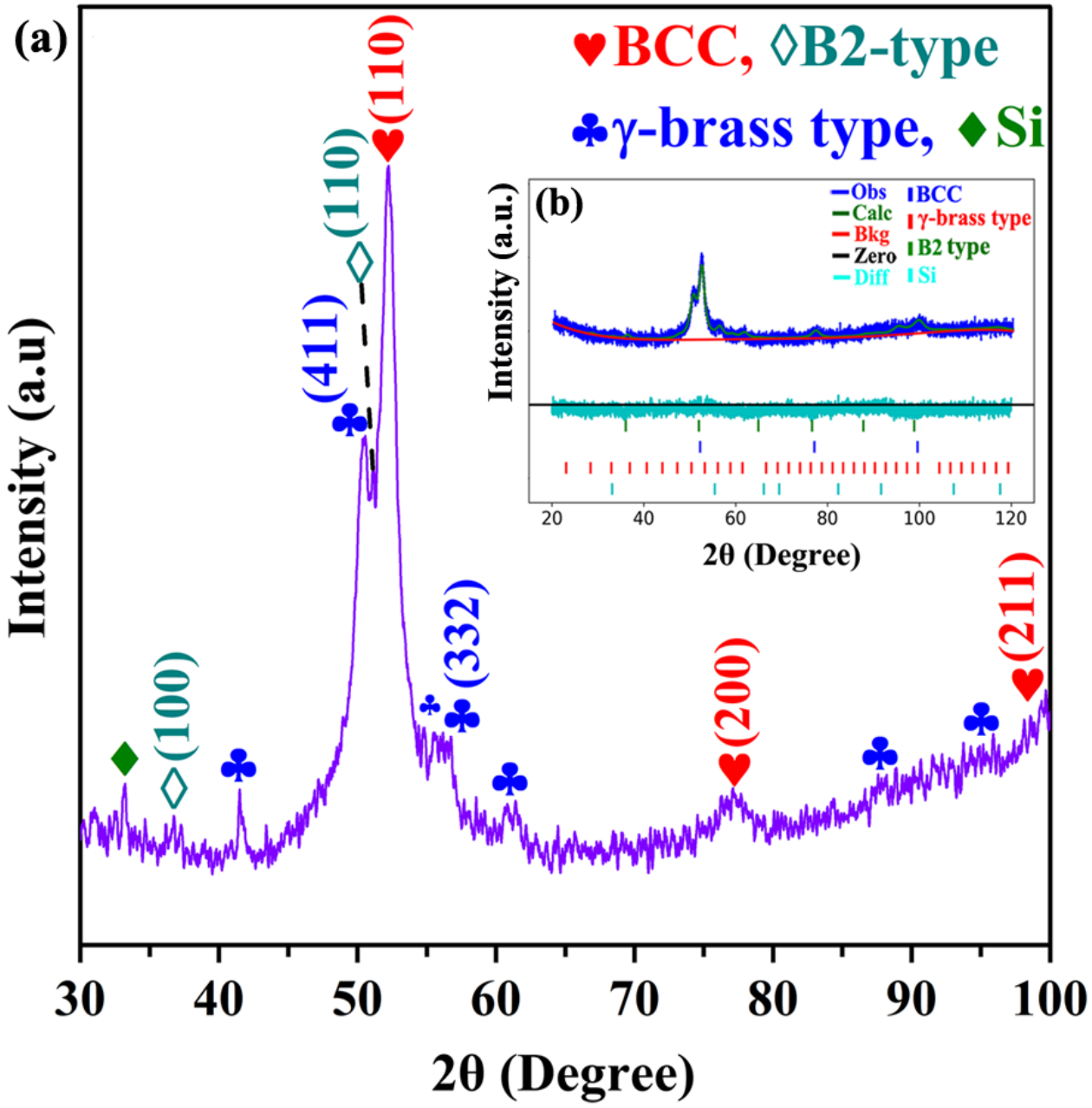

Figure 3.3: (a) XRD pattern of the 35 h milled sample; (b) Rietveld refinement of the corresponding sample. This shows the formation of the multi-phase structure (ferritic as a major phase) after 35 h of milling.

The crystallite size was found to be tuned in the range of ~13-17 nm and ~10-13 nm for BCC and γ-brass type phase, respectively. The crystallite size for Si was decreased from 20 nm to 14 nm as milling extended from 25 h to 35 h. The lattice strain was increased as the milling time

increased from 25 h to 35 h. The increase in the lattice strain with milling time is due to the atomic size difference between the individual elements, mechanical deformation in the powder particles,

Table 3.1: Variation in phase fraction, lattice strain, crystallite size and dislocation density with the function of milling time of powder sample.

Parameters	**25 h** GoF = 1.08, χ^2 = 1.18			**30 h** GoF = 1.14, χ^2 = 1.29			**35 h** GoF = 1.10, χ^2 = 1.22			
	BCC	**γ-brass type**	**Si**	**BCC**	**γ-brass type**	**Si**	**BCC**	**γ-brass type**	**B2-type**	**Si**
Lattice Parameter (nm)	a = 0.286	a = 0.882	a = 0.538	a = 0.286	a = 0.882	a = 0.538	a = 0.286	a = 0.882	a = 0.290	a = 0.538
Phase fraction (%)	74.4	21.0	4.60	73.0	23.5	3.5	64.0	27.0	6.0	3.0
Crystallite Size (nm)	17	13	20	15	12	13	13	10	13	14
Microstrain ($\times 10^{-4}$)	10849	13731	10106	13195	15445	13044	17013	18829	15052	18546
Dislocation density (m^{-2}) ($\times 10^{18}$)	1.94	---	---	2.67	---	---	3.97	---	---	---

and an increase in the fraction of grain boundary. Peak broadening and the decrease in diffraction peak intensity with the milling are also evident in Figure 3.2(a and b). The reason might be due to

the lattice distortion during the milling, which leads to induced lattice strain and grain refinement. The usual characteristics of the milling process and the combination of each phenomenon contributes to the peak broadening. There is a slight variation in the amount of phase fraction for the BCC, γ-brass type structure with the milling time was observed. The dislocation density shows the negligible change with the milling and the values are displayed in Table 3.1.

3.3 Morphology and chemical analysis of $Fe_{40}Mn_{19}Ni_{15}Al_{15}Si_{10}C_1$ HES powder

Figure 3.4(a-d) illustrates the size, shape, and morphology of the milled powder samples at different milling times. The size and shape of the powder particles were random and bulky at the early duration of the milling (as seen in Figure 3.4(a)) and became finer and more homogenous as the milling time increased.

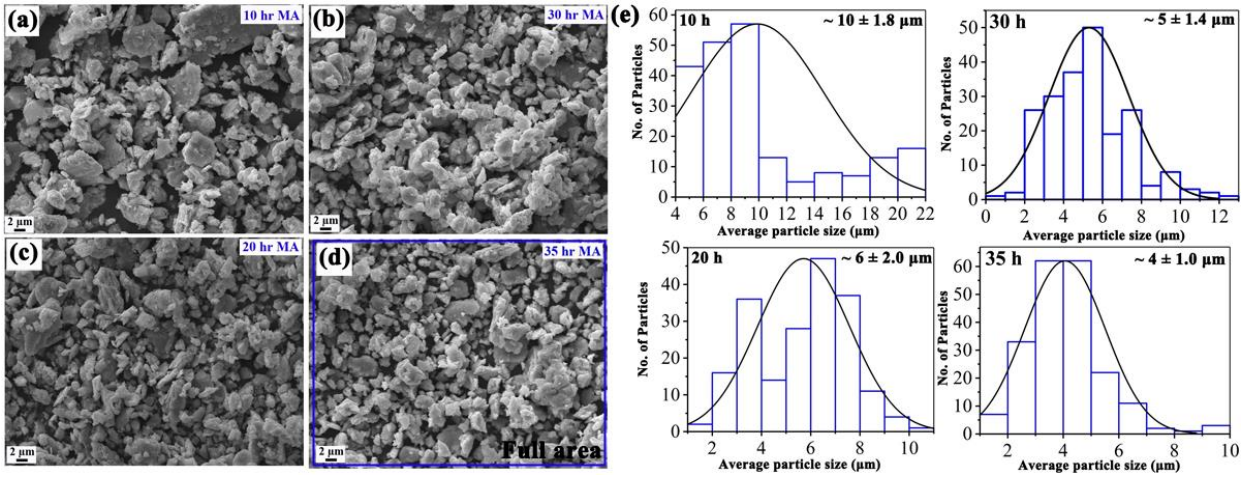

Figure 3.4: (a-d) SEM micrographs of powder samples milled at different milling time; (d) also marked the full area for EDS analysis; (e) Histograms showing the distribution of the particle size of milled samples at 10 h, 20 h, 30 h and 35 h, respectively. The histogram shows the distribution of the powder particle with the milling time. The average powder particle decreases with the prolongs milling time.

The average particle sizes decreased drastically after 20 h of milling. For 35 h milled samples, the mean particle size was 3-5 µm and the size and shapes of the particles were random. Figure 3.4

(d) also marked for full area EDS analysis, and its value is listed in Table 3.2. Figure 3.4(e) illustrates the histogram of particle size distribution at 10 h, 20 h, 30 h, and 35 h, respectively. EDX compositional surface area mapping was done on the green compact sample to investigate the elemental distribution, and a characteristic map is shown in Figure 3.5.

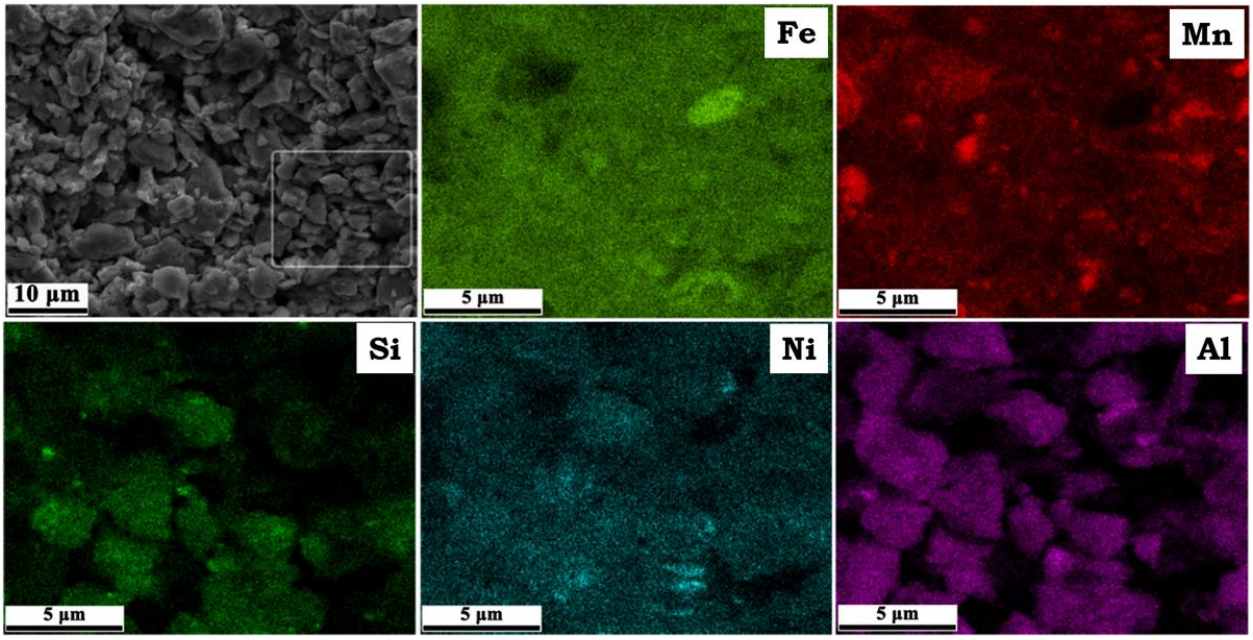

Figure 3.5: Area elemental mapping of the 35 h green powder sample.

Table 3.2: Elemental composition of 35 h milled powder samples at full area EDS.

Elemental composition (at%)						
Sample condition	**Scan area**	**Fe**	**Mn**	**Ni**	**Al**	**Si**
35 h milled powder	Full area	40.92	19.58	14.21	13.94	11.35

Predominately, two different contrast regions were evident, one is Fe rich corresponding to the BCC phase and the other is Mn rich corresponding to gamma brass type structure. All the elements were well distributed, representing the high homogeneity in the sample. So, this also confirmed the formation of BCC and gamma brass type structure in a 35 h milled powder sample.

3.4 TEM analysis of milled powder sample

The phase analysis and nanostructured nature of the 35 h milled powder samples were studied using the transmission electron microscope (TEM). The bright-field image and its corresponding selected area diffraction pattern are shown in Figure 3.6(a and b), respectively. The images showed that the nanocrystalline grains formed after 35 h milled powder. The dark patches seen in the bright images may be attributed to strain accumulation during the mechanical alloying to 35 h. It was also substantiated by Table 3.1, that the lattice strain was relatively high for the BCC phase. The formation of a ring pattern shows the polycrystalline nature of the alloy. The ring diffraction pattern corresponds to the BCC crystal structure. The diffraction rings are indexed as (110), (200), and (211) planes of the BCC phase which can be identified from the ring patterns. This BCC phase structure is very well correlated with the X-ray diffraction pattern of the 35 h milled powder sample. The dark field image was recorded from the (110) planes, as shown in Figure 3.6(c). This image also confirms that the nanostructured grains were formed after 35 h of milling, and its grain size is found to be ~ 14 nm in size. This observation was also ascertained from the Rietveld refinement of the as milled powder (listed in Table 3.1).

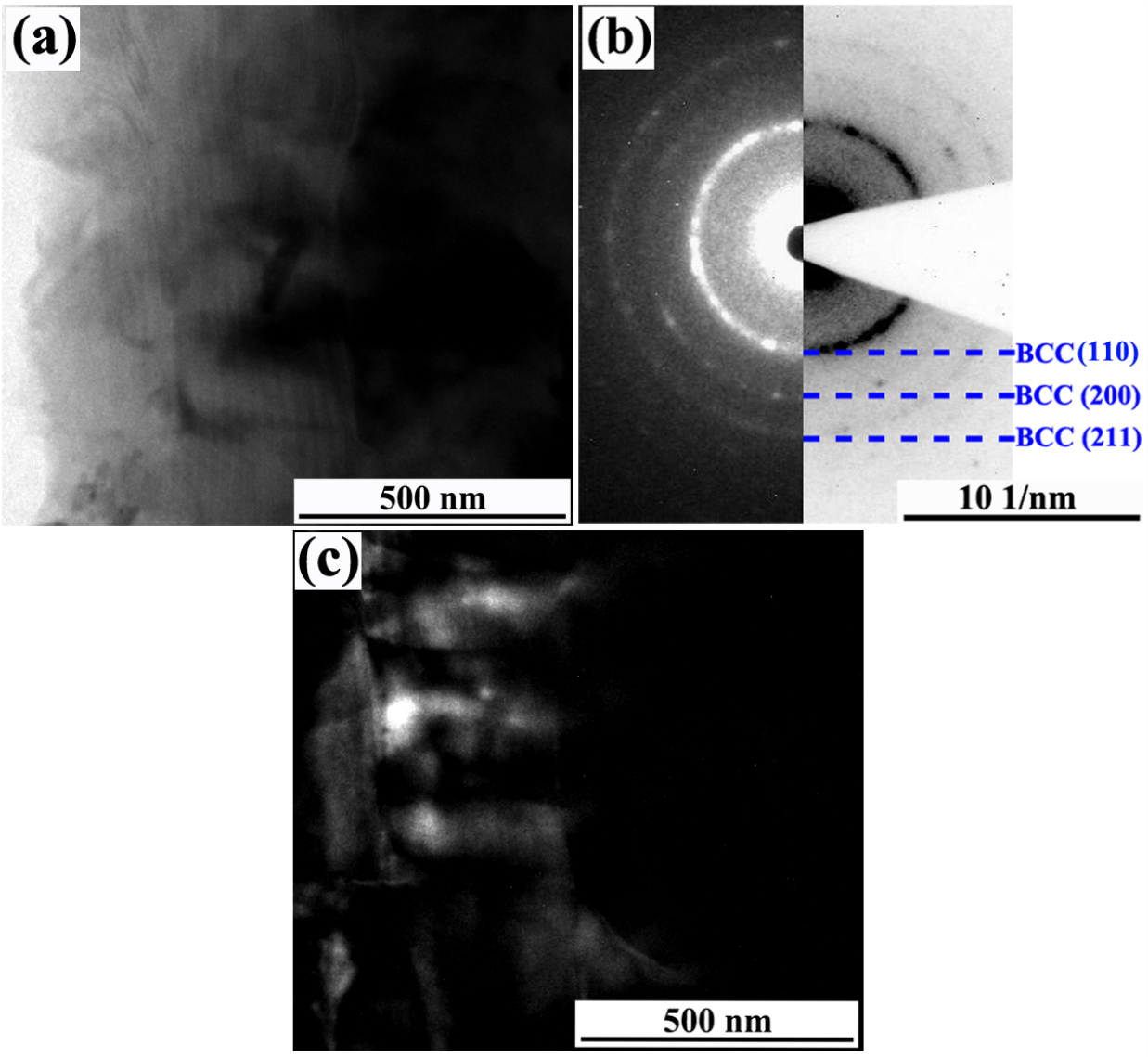

Figure 3.6: (a) The TEM bright-field image of the 35 h milled sample; (b) its corresponding selected area diffraction ring pattern; (c) Dark field image taken along the (110) plane. Polycrystalline ring pattern corresponds to the BCC phase.

3.5 Thermal stability of the milled powder sample

The thermal stability and phase transformation of high entropy steels were investigated with the help of differential scanning calorimetry (DSC). The DSC experiment was done in the temperature range of 200 ℃ - 1000 ℃ with a 20 K/min heating rate, as displayed in Figure 3.7. The milled sample was found to be thermally stable up to ~400 ℃ and beyond that it showed the two

exothermic heating events at 420 ℃ and 520 ℃. To substantiate the phase transformation to each exothermic event, annealing was done at different temperatures of 400 ℃, 500 ℃, and 600 ℃ with holding time of 1 hr. Further, XRD analysis was done to understand the sequence of phase evolution corresponding to each exothermic heating event. The ex-situ XRD of the annealed powder samples is displayed in Figure 3.8(a). The deconvolution of phases along the (110) peak of BCC phase for samples annealed at 500 ℃, and 600 ℃, is illustrated in Figure 3.8(b and c), respectively.

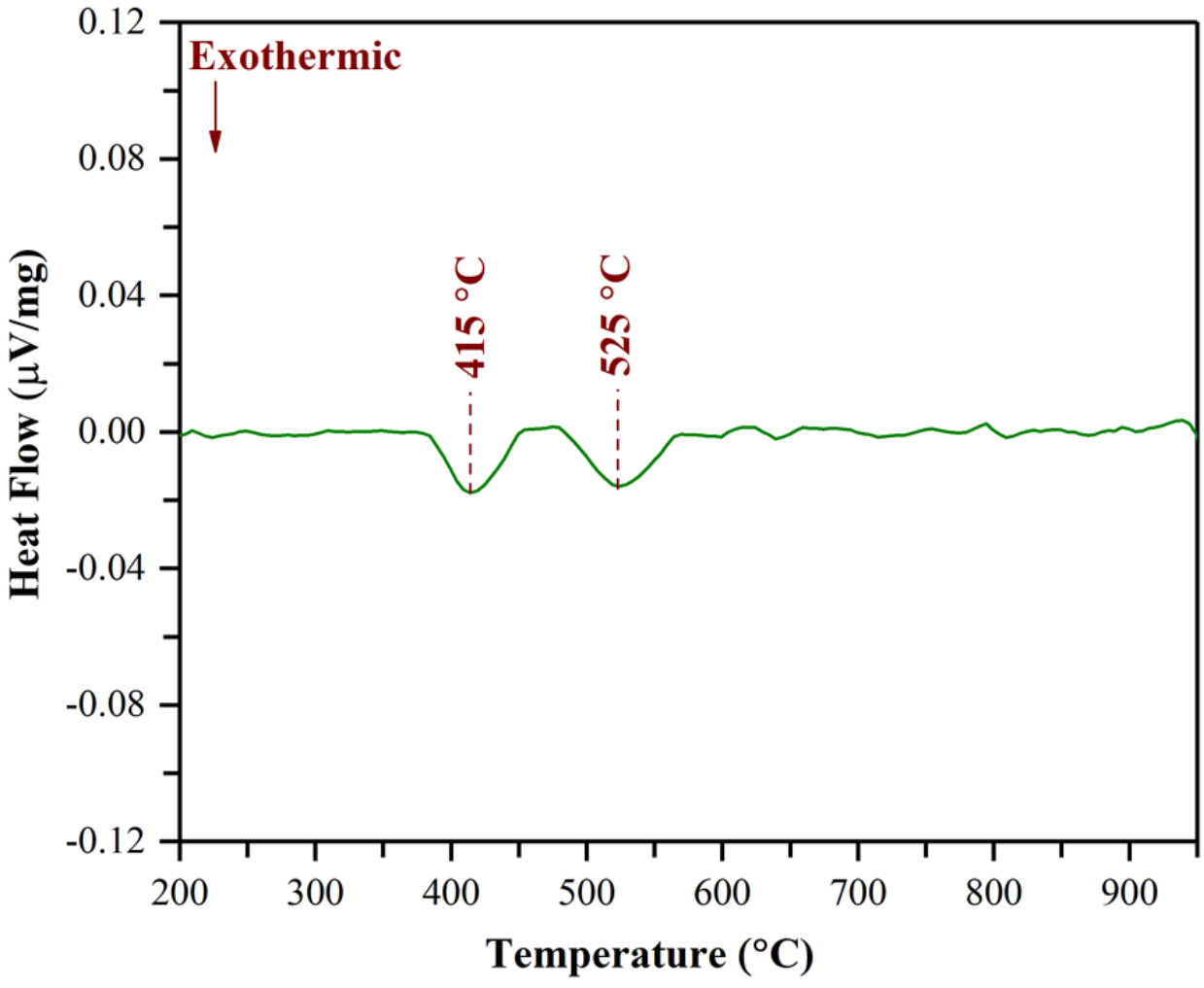

Figure 3.7: DSC thermogram of milled powder sample of the high entropy steel from 200 ℃ to 1000 ℃.

The exothermic heating event observed at ~ 420 ℃ may be corresponding to the ordering and/ or texturing of the γ-brass type phase (Figure 3.8(a and b)). The heating event at ~ 520 ℃ corresponds to the formation of Fe_5Si_3-type intermetallic (Figure 3.8(a and c)). It is clear that 35 h milled powder is thermally stable up to 400 ℃, and afterward, the diffraction peaks of the Fe_5Si_3 type intermetallic phase (a = b = 0.687 nm, c = 0.471; hP16) evolved at 600 ℃. The lattice parameter, phase fraction, and crystallite size of the various annealed sample and SPSed sample calculated using the Reitveld refinement are listed in Table 3.3.

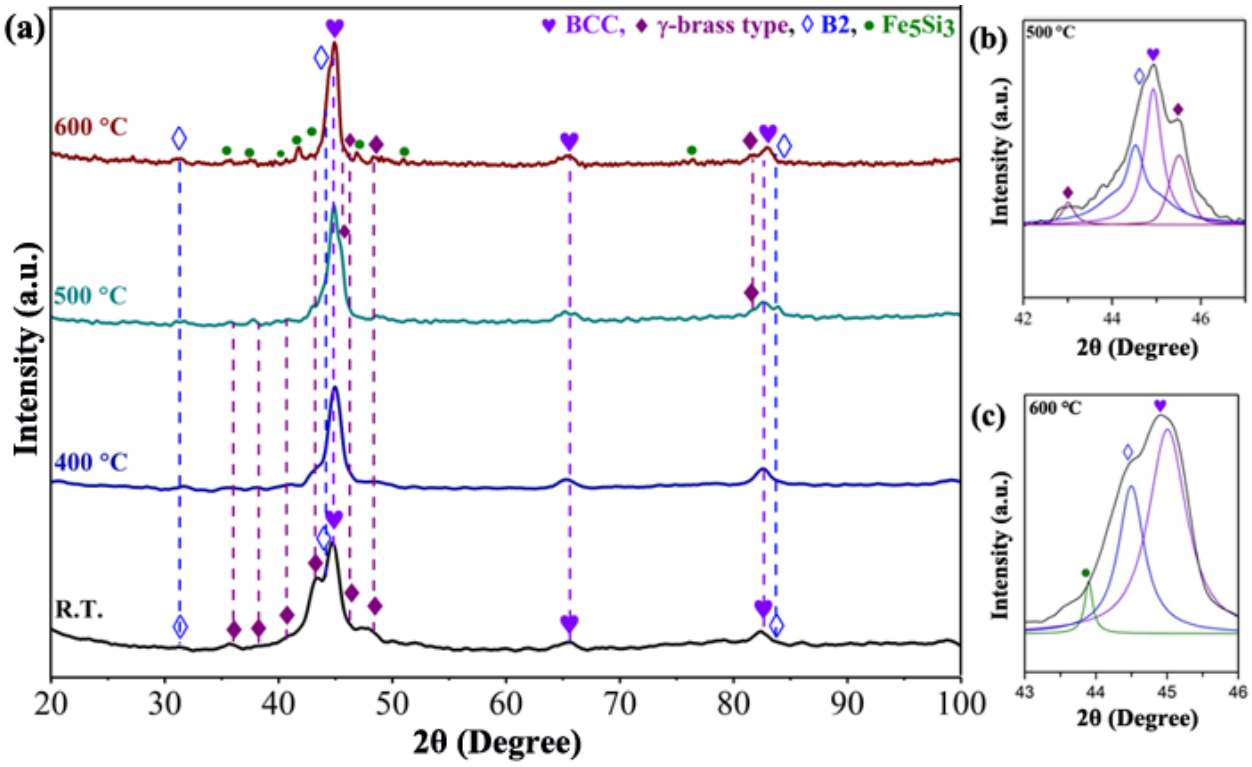

Figure 3.8: (a) Ex-situ XRD diffraction pattern of the milled sample at R.T., 400 ℃, 500 ℃, and 600 ℃; (b-c) Deconvoluted peaks for the 500 ℃ and 600 ℃, respectively. The formation of Fe_5Si_3-type intermetallic phase is correlate with exothermic event at 520 ℃.

Table 3.3: The phase fraction, lattice parameter and crystallite size of the annealed sample at 400 ℃, 500 ℃, 600 ℃, and SPSed samples of the HES1.

Condition	Phases	Phase fraction (%)	Lattice parameter (nm)	Crystallite size (nm)
400 ℃; GoF = 1.05, χ^2 = 1.10	BCC	57.00	0.286	21
	γ-brass type	21.30	0.882	12
	B2	21.70	0.290	22
500 ℃; GoF = 1.04, χ^2 = 1.07	BCC	47.70	0.286	23
	γ-brass type	36.30	0.882	16
	B2	16.00	0.290	25
600 ℃; GoF = 1.18, χ^2 = 1.40	BCC	43	0.286	26
	γ-brass type	3.00	0.882	19
	B2	38.50	0.290	29
	Fe_5Si_3 type	15.50	a = b = 0.687, c = 0.471	18
SPSed; GoF = 1.33, χ^2 = 1.78	BCC	56.00	0.286	22
	B2	34.00	0.290	18
	γ-brass type	1.60	0.882	21
	Fe_5Si_3 type	8.40	a = b = 0.687, c = 0.471	19

3.6 Structural and microstructural analysis of SPSed sample

XRD pattern of the SPSed sample is displayed in Figure 3.9(a), and its deconvoluted image in the 2θ range of 51º - 54º is shown in Figure 3.9(b).

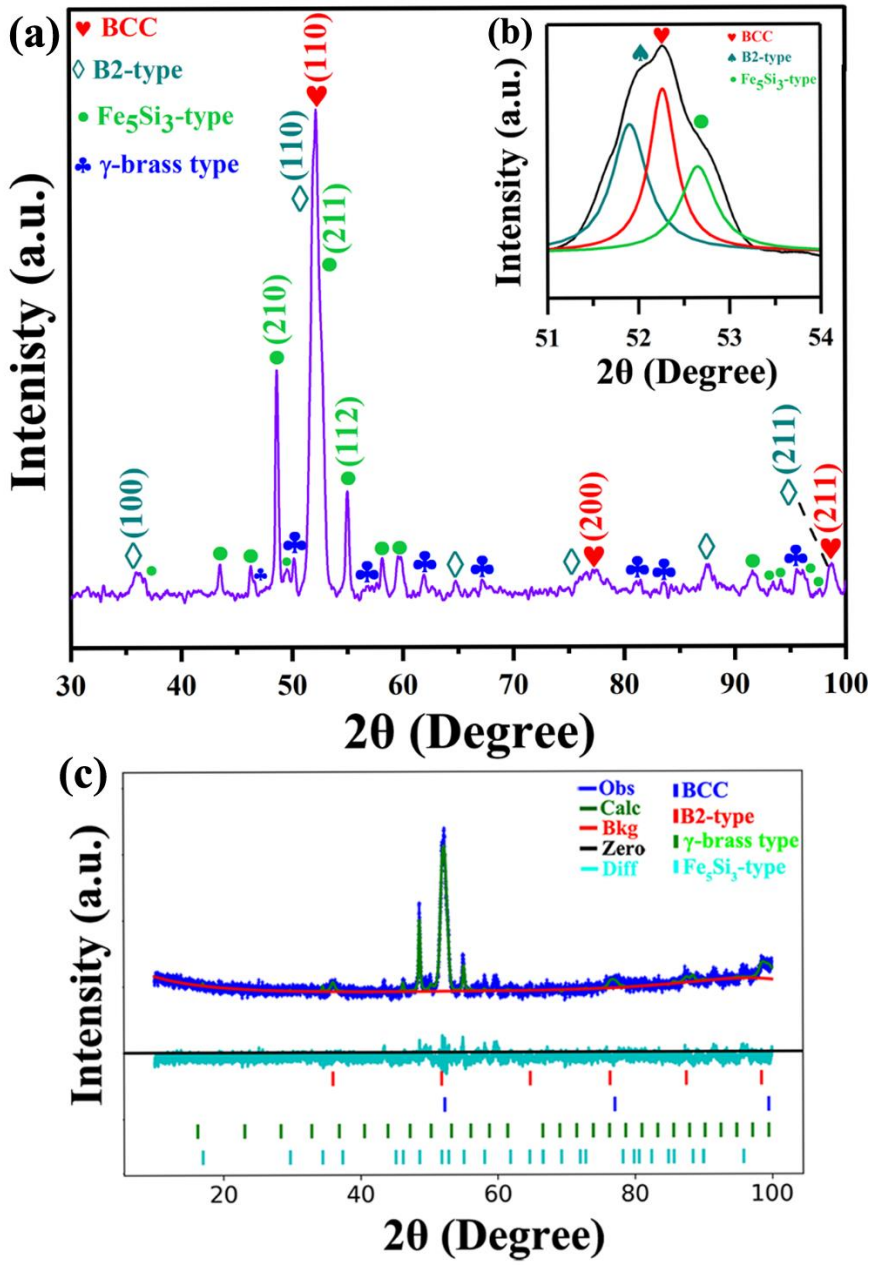

Figure 3 9: (a) XRD pattern of the SPSed pellet; (b) Deconvolution of the SPSed sample ranging from 51º- 54º; (c) Rietveld refinement plot of the SPSed pellet. The ferritic (BCC) type high entropy steel with B2, γ-brass type structure and Fe_5Si_3 type intermetallics can be depicted.

The BCC (ferrite) phase was observed as the major phase and secondary phase as B2-type along with the Fe_5Si_3 type silicide and trace amount of γ-brass type phase as precipitates. Figure 3.9(c) shows the Rietveld refinement of the SPSed sample confirming the presence of BCC, B2-type, γ-brass type, and Fe_5Si_3 type silicide. The SEM micrographs of the SPSed sample at 900 °C and 50 MPa with different magnifications are displayed in Figure 3.10(a-b), exhibiting different contrasts i.e., white, black, light, and dark grey, which may correspond to the BCC, B2-type, γ-brass type and Fe_5Si_3-type silicide, respectively.

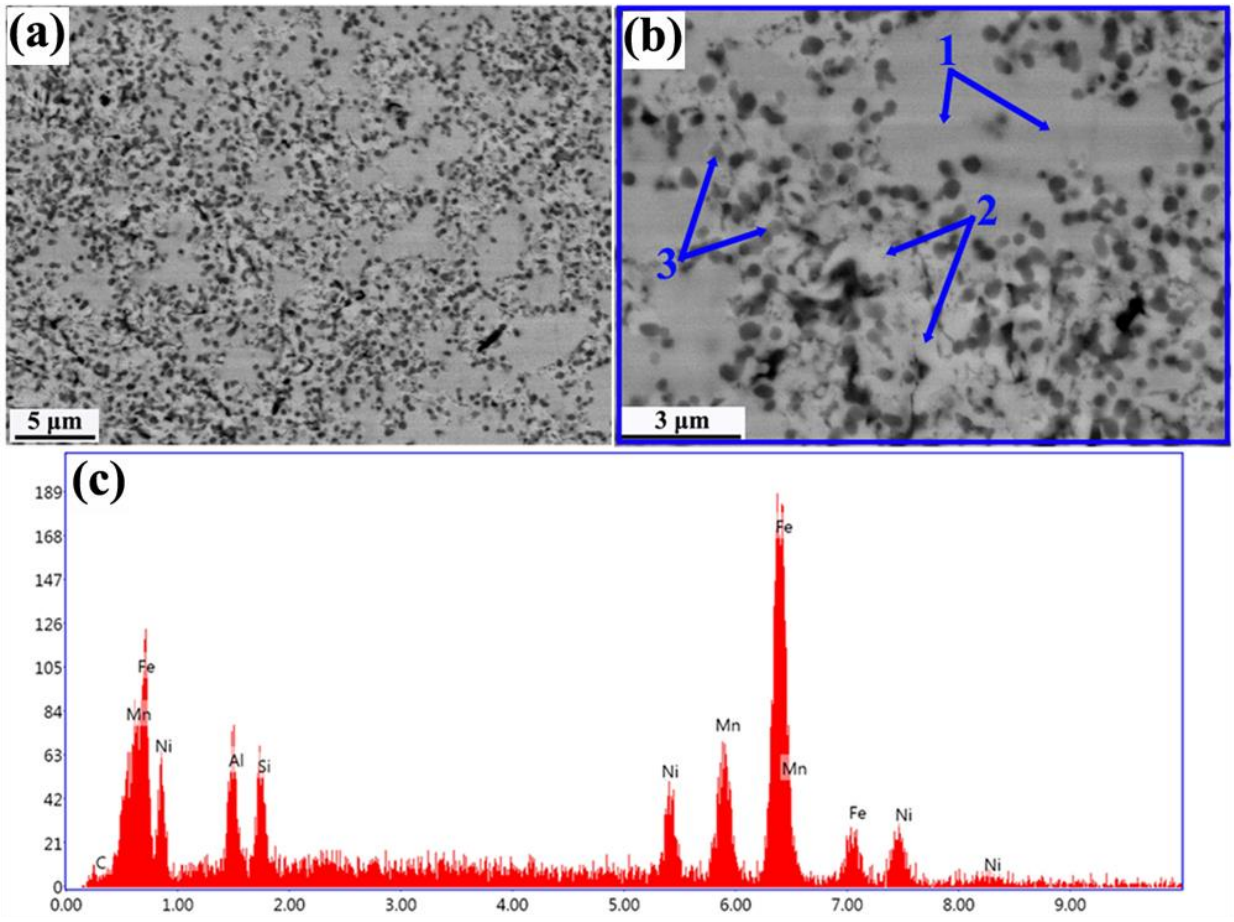

Figure 3.10: (a and b) SEM image of the SPSed sample of the non-equiatomic high entropy steel at different magnifications; (c) Full area EDS analysis of the marked area (in (b)). The different contrast i.e., white (2), light grey (1), dark grey (3) contrast are clearly visible in SEM images.

The SEM-EDS at full-area of the SPSed pellet is shown in Figure 3.10(c). The presence and distribution of all the elements in an SPSed pellet of non-equiatomic high entropy steel is uniform and chemically homogeneous. The BSE image and the EPMA elemental mapping of the SPSed sample reveal the multi-phase nature of the non-equiatomic high entropy steel, as illustrated in Figure 3.11. The different contrast features are clearly visible in the BSE image i.e., white, light grey, and evenly distributed dark grey particles. The point WDS analysis of these SPSed samples revealed that the white contrast was found to be rich in Al and Ni, which correspond to the B2-type phase (spot 1). The light grey contrast was found to be rich in Fe, Mn, and Ni, corresponding to the BCC (ferritic) phase (spot 2). The values of the point WDS analysis of the elemental weight percentages are listed in Table 3.4. Figure 3.11 displays the EPMA elemental maps of Fe, Mn, Ni, Al, and Si. It can be discerned that the Fe, Mn, and Ni were found to be uniformly distributed in the matrix owing to the existence of the major BCC phase. The high X-ray intensity regions corresponding to Al have a slightly higher intensity of Fe and Ni, which may be attributed to the presence of the B2-type phase. Similarly, the region enriched with Si shows the presence of a Fe_5Si_3-type phase. It is very difficult to distinguish the regions corresponding to the γ-brass type phases. This can be corroborated well with the XRD results owing to the very low phase fraction of γ-brass type phases in SPSed samples. The EMPA elemental mapping helped in the understanding and presence of the multi-phase microstructure in this HES prepared by SPS (Figure 3.9(a)).

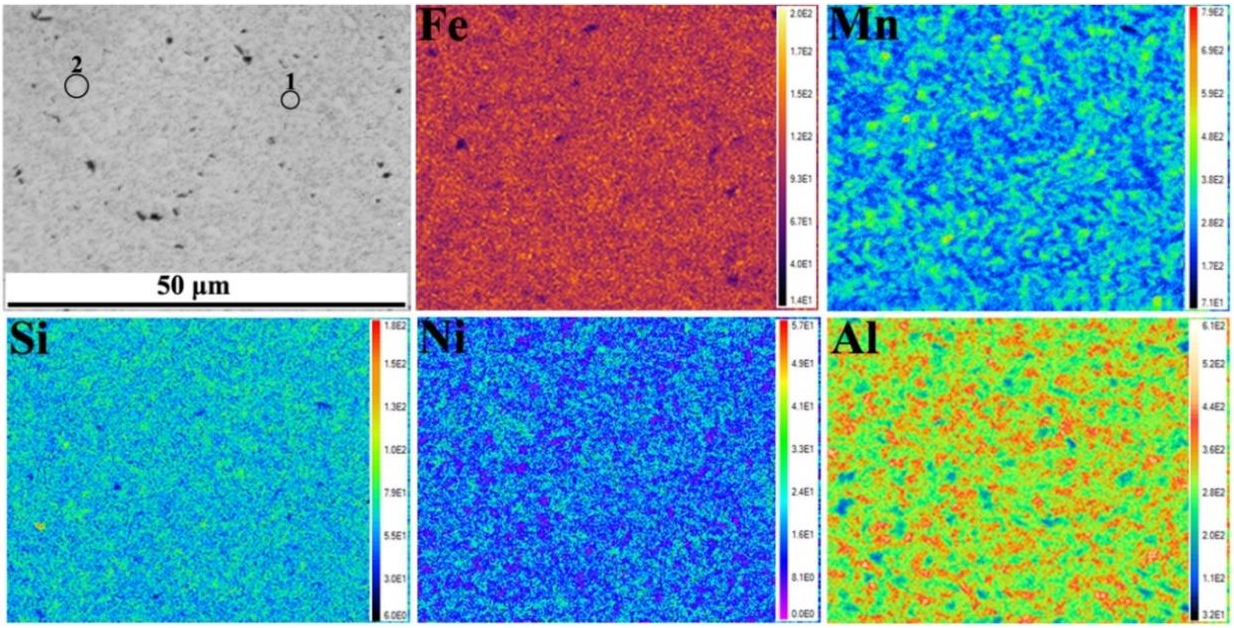

Figure 3.11: BSE image and EPMA elemental mapping of SPSed sample.

Table 3.4: Elemental composition of SPSed sample of the HES1 at full area EDS and point WDS.

		Elemental composition (wt.%)				
Sample condition	**Scan area**	**Fe**	**Mn**	**Ni**	**Al**	**Si**
SPSed sample	**Full area**	46.82	20.56	18.25	8.94	5.18
	Spot 1	32.46	10.00	32.09	21.82	2.63
	Spot 2	44.53	21.60	20.66	7.33	5.88

3.7 Physical and mechanical properties of SPSed sample

The consolidated pellet was found to have a relative density of ~ 99.5 %, which was calculated using equation 2.3, and the theoretical density was computed by the rule of mixture (6.55 g/cc). The experimental density was calculated using the Archimedes principle (equation 2.4). The experiment was repeated six times to calculate the average experimental density (6.49 ± 0.3 g/cc).

The load-displacement curve of the SPSed pellet of high entropy steel, is illustrated in Figure 3.12(a). The nature of the p-h curve depicts the presence of limited plasticity in these SPSed samples. The depth of indentation for the SPSed samples was found to be ~5.08 µm. Figure 3.12(b) shows the optical image of the indent on the surface of the SPSed pellet. The optical micrograph shows no evidence of crack formation even at a load of 5000 mN. Figure 3.12(c) displays the compressive stress-strain plot of the SPSed sample. The evaluated values of the

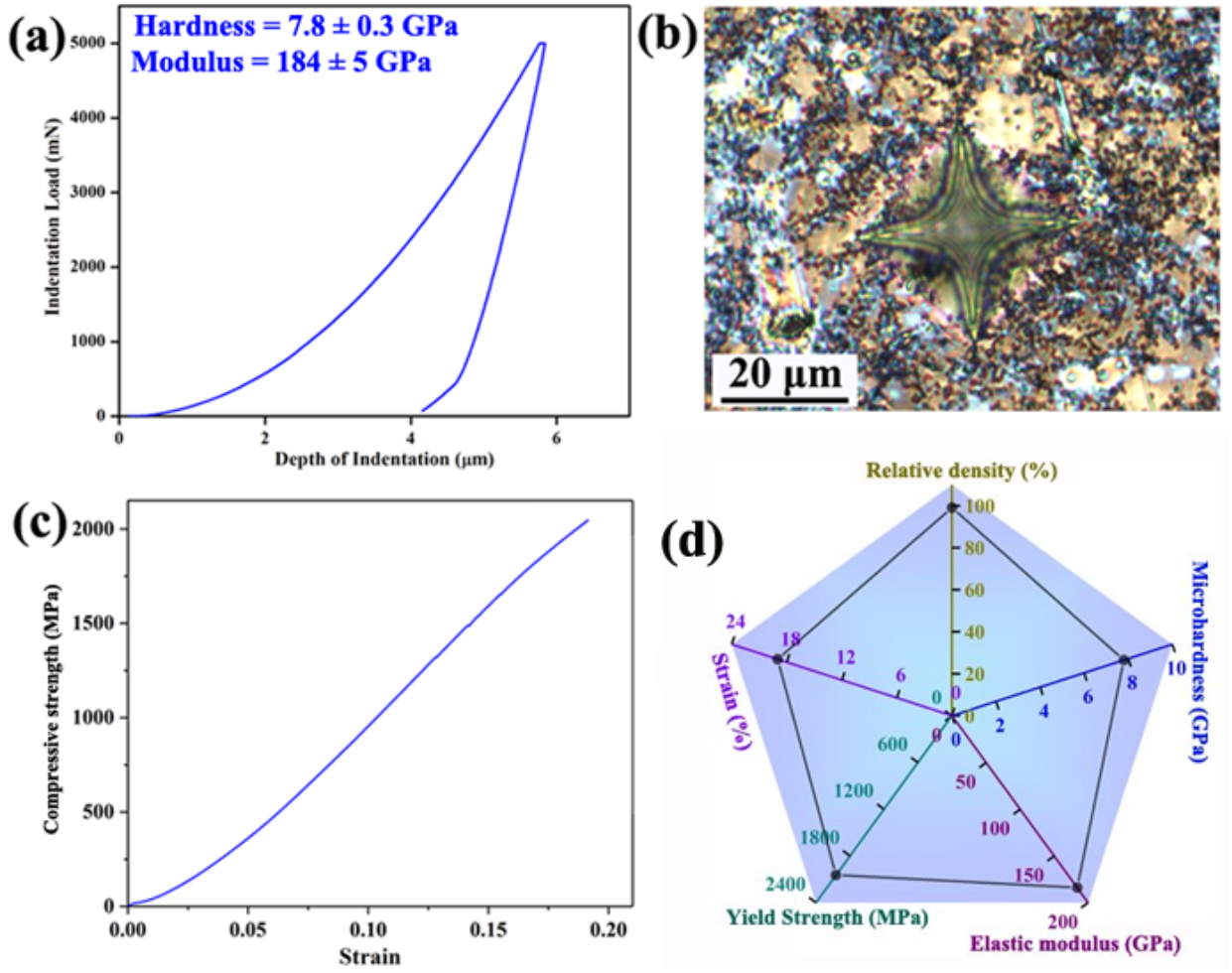

Figure 3.12: (a) Depth of penetration vs Indentation load; (b) Optical micrograph of the indentation spot; (c) Compressive engineering stress and strain curve; (d) Radar diagram. This illustrates the physical and mechanical properties of the SPSed pellet.

average microhardness and elastic modulus of the SPSed pellet are observed at ~7.8 ± 0.3 GPa and 184 ± 5 GPa, respectively. Figure 3.12(d) shows the radar diagram of the SPSed pellet revealing the physical and mechanical properties. The evaluated values of the average ultimate compressive strength and strain of the SPSed pellet are 2000 ± 200 MPa and 19%, respectively.

SEM (SE-mode) micrograph at different magnifications for the fractured sample of high entropy steel, is displayed in Figure 3.13(a, b, c, and d).

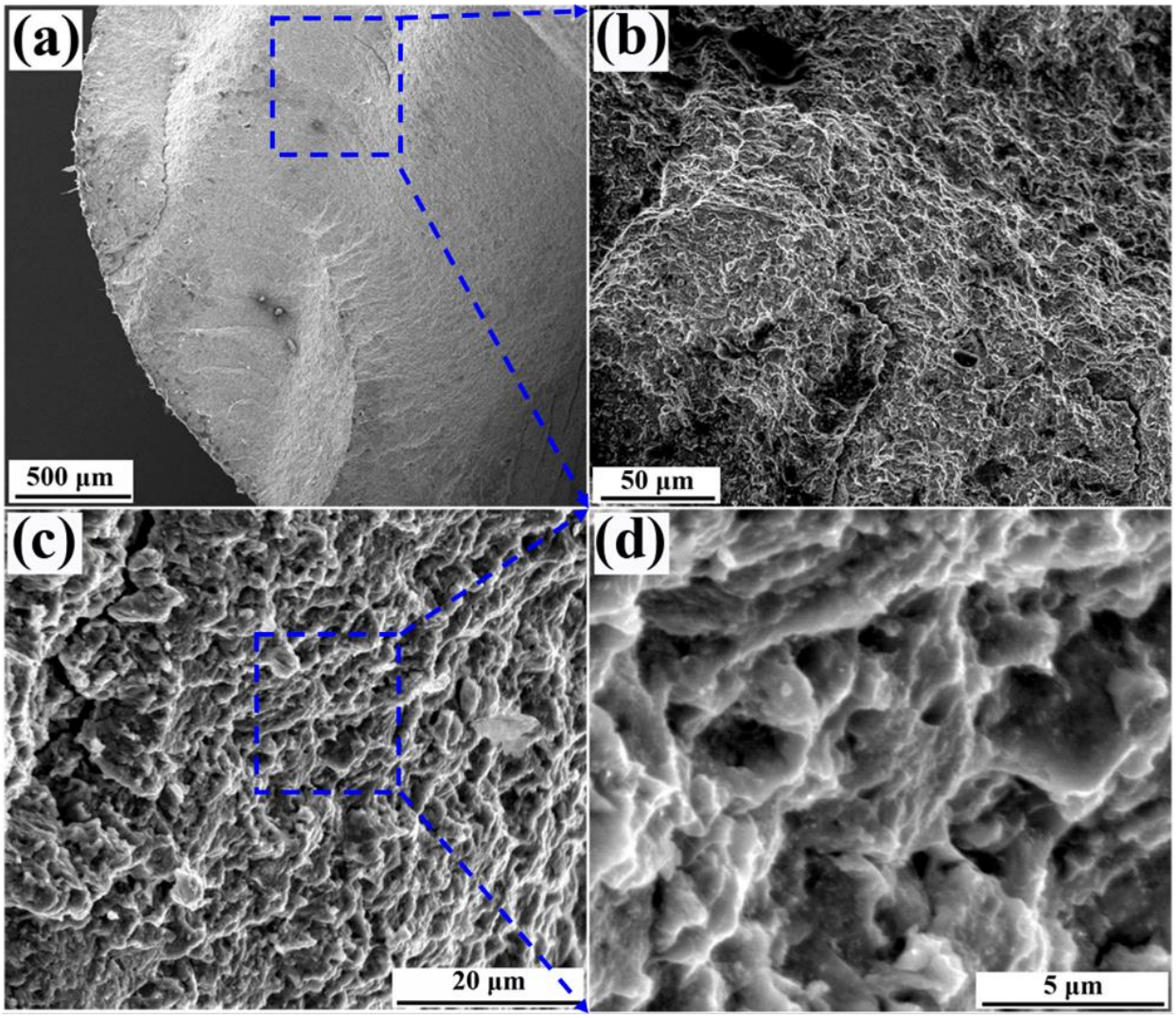

Figure 3.13: (a, b, c, and d) SEM (SE) micrograph at different magnification of the fractured surface of SPSed sample of the HES1.

The different types of fractured morphologies can be ascertained from the Figure 3.13 (c, and d). The micropores-like features were uniformly distributed in the fractured surfaces, which would be of the same sizes as the precipitates (Fe_5Si_3-type) formed after the SPS. However, the fractography have both brittle and ductile features i.e., crack and shallow dimple are observed in the Figure 3.13 (c, and d). These differences in fractured patterns are due to the dual-phase structures formed in the SPSed samples. The brittle kind of fractured morphologies are observed such as cracks, signifying high strength, and ductile kind features are seen such as shallow dimples suggesting ductility in the high entropy steel.

3.8 Sliding friction and wear behaviour of the SPSed sample

The coefficient of friction (CoF) of HES1 was determined with the help of a reciprocating sliding wear test under dry conditions at room temperature. The average CoF was taken as the tangential load by the constant applied normal load, which was recorded with time. The curve between CoF vs time at different load conditions of 5 N, 10 N, and 20 N with a constant frequency of 10 Hz are illustrated in Figure 3.14(a). The CoF was found to be 0.15 ± 0.02, 0.47 ± 0.04, and 0.72 ± 0.05 at load conditions of 20 N, 10 N, and 5 N, respectively for the SPSed samples of high entropy steel. It is evident from Figure 3.14(a) that the fluctuation in the CoF curve under 5 N and 10 N load might be attributed to the accumulation and segregation of wear debris during the wear cycle. The CoF under the load conditions of 5 N and 10 N showed two types of behaviour, firstly CoF increased at the early period of cycles, which might be due to the indenter settling and the breaking-in of the surface against the hard ceramic (Al_2O_3) counterpart, and then gradually decreased and eventually reached to a steady state condition. This kind of fluctuation in CoF is common under lower load condition ($\leq$ 20 N) in the HEAs [233]. The CoF curve is steady under the load condition of 20 N (Figure 3.14(a)). The increase in CoF under lower load condition was

due to the wear debris accumulating on the worn surface and it decreased under higher load condition (20 N). The friction coefficient decreases with increase in the normal load, which may be due to the fracturing of some of the asperities, decreasing surface roughness for the counter surfaces [233]. Additionally, some debris are crushed as plate-like materials and patched on the surface, decreasing the frictional force [234]. This kind of trend of CoF with increasing normal load are also observed in other metallic alloy systems [234,235]. Figure 3.14(b) shows the value of CoF and specific wear rate under load conditions of 5 N, 10 N, and 20 N, which shows that the CoF decreased with the increase in load condition, whereas the specific wear rate showed inverse trend with applied load. The wear rate was calculated using the equation 2.5. The specific wear rate values for SPSed samples of high entropy steels were found to be 1.79 x 10^{-5} mm^3/mN, 3.12 x 10^{-5} mm^3/mN, and 4.36 x 10^{-5} mm^3/mN under loads of 5 N, 10 N, and 20 N, respectively. This type of normal load dependence on the wear behaviour was also seen in the previously reported HEAs [236].

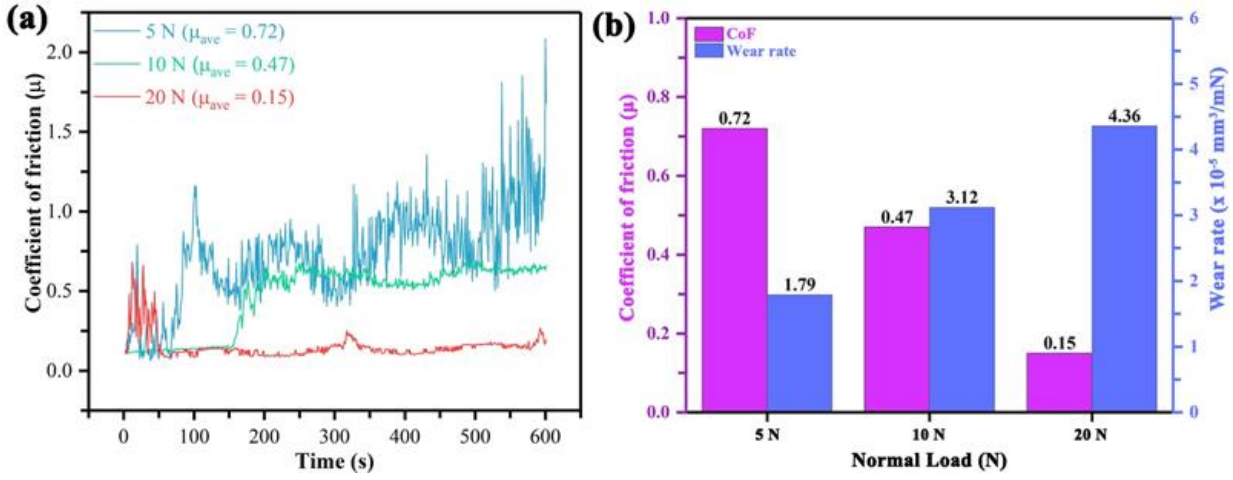

Figure 3.14: (a) Change in coefficient of friction (CoF) as a function of time (s) during sliding wear under the various normal load i.e., 5 N, 10 N and 20 N at 10 Hz frequency for SPSed sample; (b) Average coefficient of friction and specific wear rate against the various normal applied load i.e., 5 N, 10 N and 20 N.

3.9 Worn surface morphology of the SPSed samples

To understand the wear mechanism in non-equiatomic high entropy steel a detailed examination of the worn surface was done using the SEM. SEM micrographs at different magnifications under the load of 20 N, 10 N, and 5 N, are displayed in Figure 3.15(a and b), (c and d), and (e and f), respectively. Figure 3.15(c, d, e, and f) show the worn surface morphology under the load of 10 N and 5 N. It is clearly visible in the SEM images that the parallel shallow grooves were developed along the direction of the sliding wear track. The scratches were also evident in the wear track, which was formed due to the ploughing of micro-asperities between the two friction surfaces. This kind of feature is related to the abrasive wear mechanism. Further, the fine wear debris and discontinuous glaze layers were also visible on the worn surfaces. All these features are marked by the black arrows in Figure 3.15(a, c, e, and f). The fluctuations in the CoF curve under the load condition of 5 N and 10 N was due to the homogenous distributions of wear debris and glaze layer. Figure 3.15(a and b) displayed the worn surface of the SPSed sample under 20 N load conditions. With the normal load increasing, more abrasive particles were present and involved in polishing the worn surface. At, higher load conditions the wear debris washed away from the surface plate-like materials, which leads to the patches on the worn surface, resulting in the friction force decreasing against pairs. This shows the relatively less wear debris and glaze as related to the low load conditions. Additionally, the microcracks were evident in the worn surfaces, which were perpendicular to the sliding wear direction, as displayed in Figure 3.15(a, b, c, d, e, and f). The formation of microcracks might be due to the stick-slip behaviour and localized stress during the continuous sliding wear.

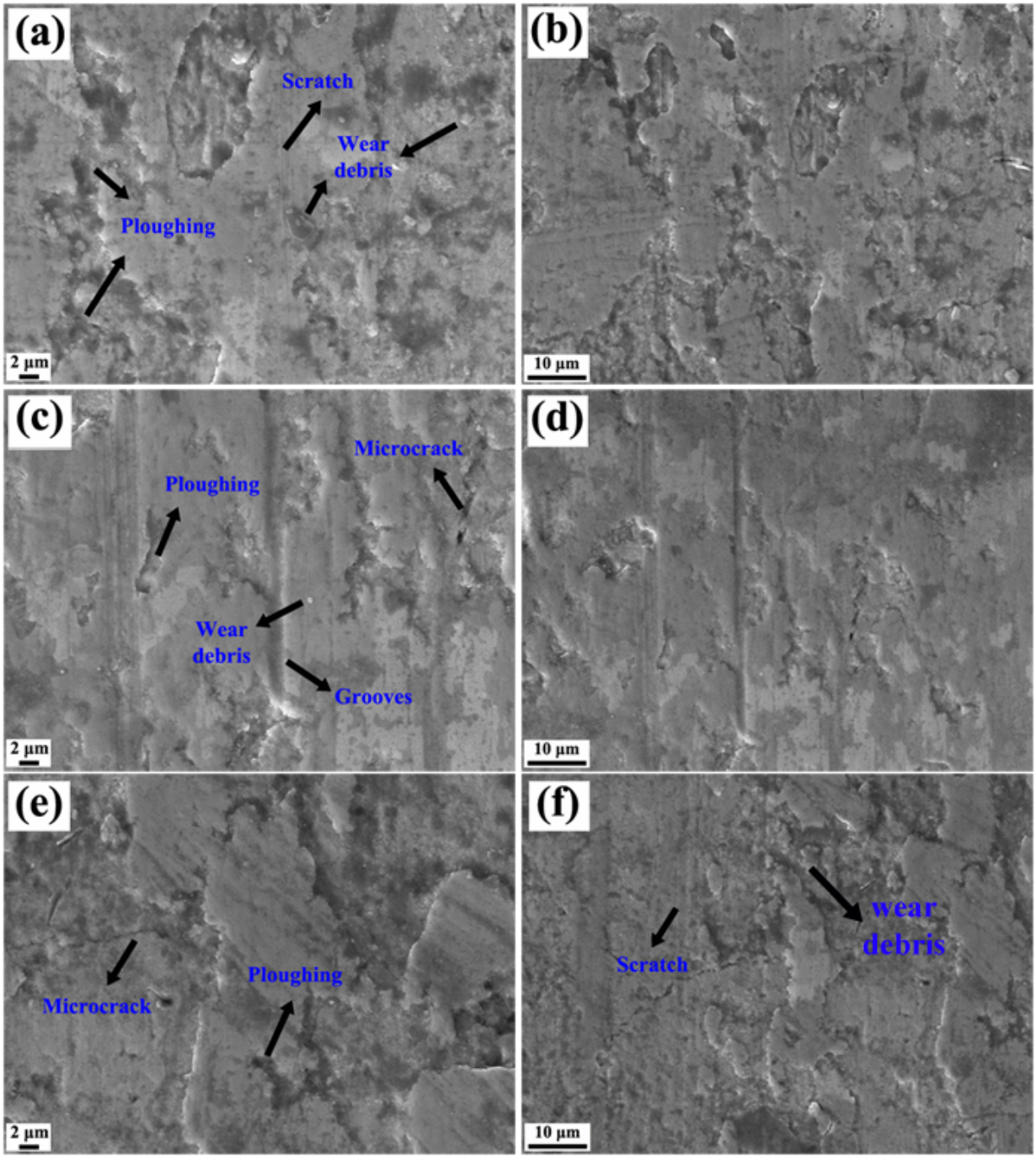

Figure 3.15: SEM (SE mode) micrographs at different magnification of wear fractured SPSed sample of the HES1; (a and b) at 20 N; (c and d) at 10 N; (e and f) at 5 N load condition.

3.10 Biocompatibility of the SPSed sample

The in-vitro biocompatibility of the SPSed sample of the high entropy steel and control (316L) was done by exposing it in the Osteosarcoma MG-63 cell, as illustrated in Figure 3.16. The MG-

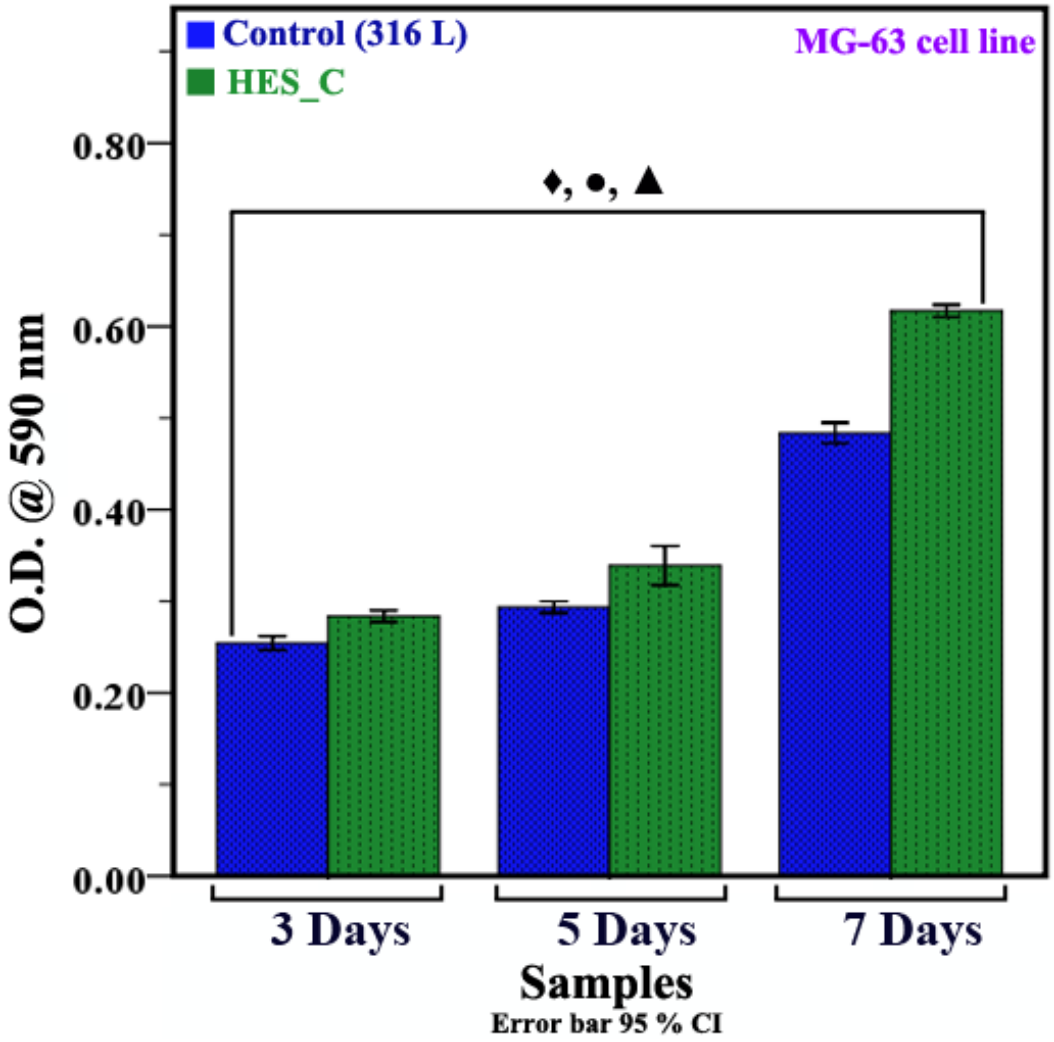

Figure 3.16: Concentration-dependent quantitative analysis (MTT assays) of mesenchymal stem cell (MG-63) on control (316L) and SPSed sample of non-equiatomic FeMnNiAlSiC HES after 3, 5 and 7 days. The symbol (♦) represents the statistically significance differences at $p \leq 0.05$ in the mean optical density (O.D.) among the SPSed sample of HES1 with the control sample (316L) treated for 3 days with 5 and 7 days. The symbol (●) represents the statistically differences in the O.D. among all the sample, treated for 5 days with respect to sample treated for 7 days. The symbol (▲) represents the statistically differences in the O.D. among the 316L with high entropy steel sample treated for 7 days.

63 was selected as a cell line due to its adherent nature, which gave an accurate in-vitro simulation result. The optical absorbance value was measured directly from the living cell viability at a wavelength of 595 nm. The cell viability of MG-63 cells on the high entropy steel sample and control were quantitatively measured in terms of cell proliferation after 3, 5, and 7 days of incubation period was measured using the equation no. 2.6, and its value are 1.11 %, 1.15 %, and 2.10%, respectively. The cell viability of the alloy increased with the increase of the incubation period. During the initial period of the incubation period of 3 and 5 days, the mean optical density ($p \leq 0.05$) of high entropy steel is not that significantly different from that of the control. However, for the incubation period of 7 days, the mean optical density ($p \leq 0.05$) of the non-equiatomic HES was significantly higher as compared to the control. The mean optical density ($p \leq 0.05$) of the high entropy steel was highest for 7 days as compared to 3 and 5 days.

3.11 Discussion

3.11.1 Alloying behaviour and microstructure

The phase evolution during milling and after the spark plasma sintering was correlated with the thermodynamic parameters. The three parameters for the prediction of disordered solid solution in the HEAs i.e., high configurational entropy (ΔS_{conf}), mixing enthalpy (ΔH_{mix}), and size mismatch (δ). The ΔS_{conf}, ΔH_{mix}, and δ parameters were calculated based upon the Boltzmann hypothesis, Miedema model, and Zhang et al. [237], and their equations are given in equation no. 1.2, 1.3, and 1.6, respectively. The calculated values of the thermodynamic parameter for the non-equiatomic high entropy steel are listed in Table 3.5. The values of the various parameters are well within the range of random solid solution formation criteria. Guo et al. [83] proposed some more parameters i.e., valence electron concentration (VEC) and Ω for the prediction of solid solution

formation in the multicomponent alloys, and it is calculated using equation no.1.7 and 1.8, respectively. The VEC is used to predict the FCC/BCC or both phase formation in the HEAs.

Table 3.5: The thermodynamic parameter of the HES1.

Thermodynamic parameter	**ΔH_{mix} (kJ/mol)**	**ΔS_{conf} (J/K-mol)**	**δ (%)**	**Ω**	**VEC**
Present work	-8.4	12.4	7.6	2.0	6.92

The VEC is well within the range of both phase formations, but it forms the BCC-type structure in the milled and SPSed sample of the present alloy. The phase formation in $Al_xCoCrCuFeNi$ (x = 0.45, 1, 2.5, 5 at. %) HEAs are discussed on the basis of mixing enthalpy, configurational entropy, and size mismatch [238]. It was stated that with the increase in Al, the B2 phase was formed, which is due to the high mixing enthalpy. It is also mentioned that the enthalpy of mixing in the HEAs system was preferred to form the ordering or clustering (formations of intermetallic) [239]. Shivam et.al, [148] discussed the phase formation in the non-equiatomic $Fe_{40}Cr_{25}Ni_{15}Al_{15}Co_5$ medium entropy alloy in terms of binary mixing enthalpy and configurational entropy, which has formed the dual-phase structure i.e., BCC and ordered B2 structure. The B2 phase formation in the alloy was correlated with the binary enthalpy of mixing in Ni-Al, which is the highest among the other pairs. In the present alloy, the binary enthalpy between the Al-Fe, and Al-Ni are also highly negative. The values of the possible binary enthalpy in the present alloy system are illustrated in Figure 3.17. To retain the solid solution in the HEAs at room temperature, the configurational entropy is not sufficient. A B2-type structure in the alloy was formed due to the binary negative enthalpy. The criteria proposed for the prediction of the disordered solid solution in the HEAs are based on the results of the reported HEAs. However, some of the reported HEAs suggested that

Zhang's criteria were neither necessary nor sufficient condition to predict the formation of disordered solid solution in the HEAs. This can only provide the basic idea of predicting the phase formation criteria of a disordered solid solution. Other than the thermodynamic parameters, the processing technique and atomic percentage of the individual elements also play an important role in the phase formation of the HEAs [239].

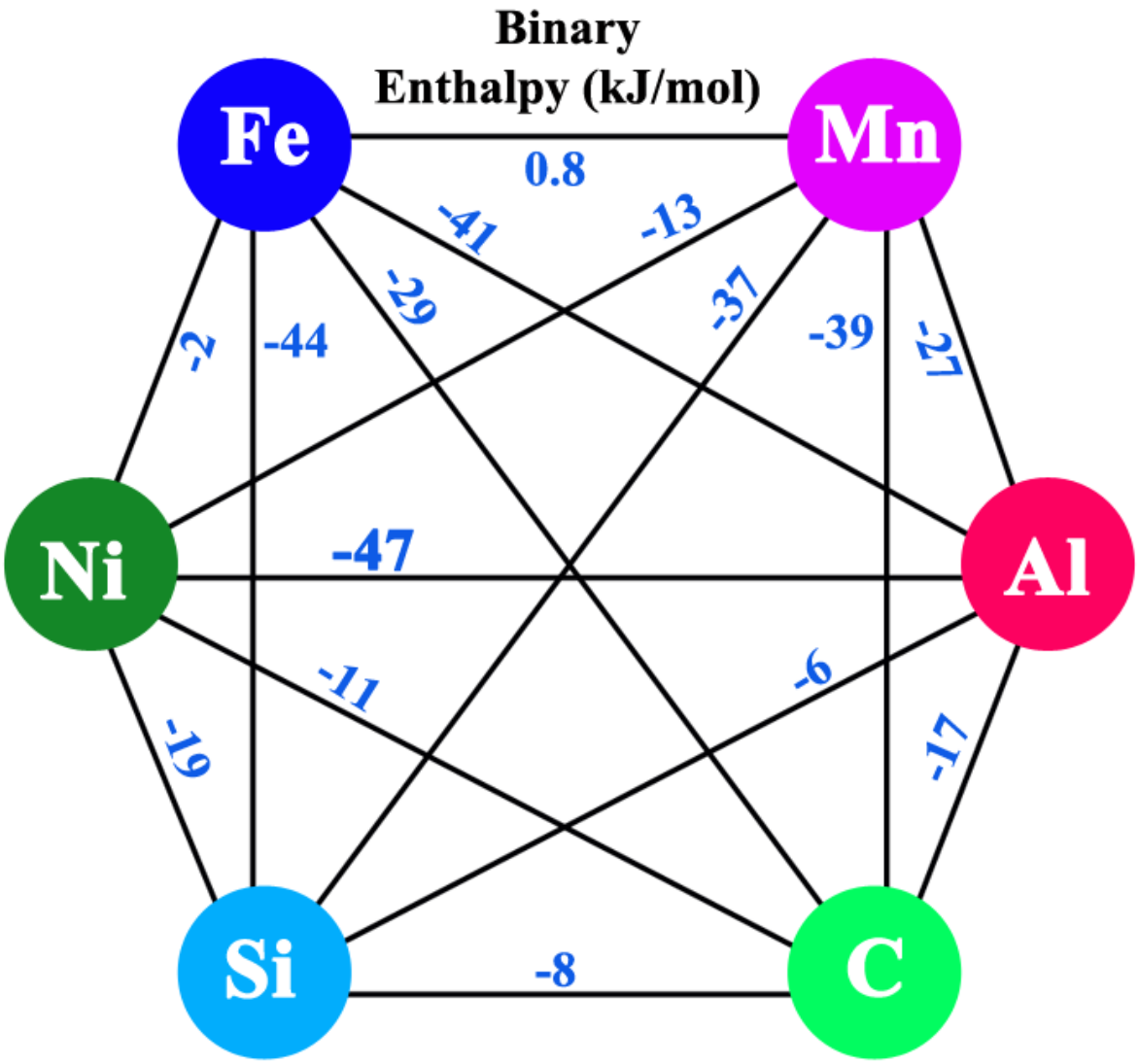

Figure 3.17: Binary enthalpy (kJ/mol) of all the binary alloys in the non-equiatomic FeMnNiAlSiC HES.

The diffraction intensity of the elemental peaks started diminishing as the milling time progressed, which ascertained that the alloying was initiated. The dissolution of the individual elements during the milling were correlated with the physicochemical properties and its value is compiled in Table 2.3. The dissolution of the elements depends on the melting points and the brittleness [240]. But, carbon, being an interstitial element dissolved faster as compared with the other alloying elements present which might be due to its less atomic size and high diffusivity of carbon compared to the other alloying elements [230, 241]. As the milling proceeded, the Al dissolved followed by Mn and Ni, and formed the solid solution. This alloying rate depends upon the melting point and self-diffusion coefficient of the individual elements [240]. Si remains undissolved after 35 h of milling due to the lowest self-diffusion coefficient and non-metallic behaviour [240]. The lattice parameter of the major BCC phase formed during the milling is close to the ferritic iron (α-Fe) (acting as host lattice). Shivam et al. [242] explained the concept of the host lattice in the HEAs system in terms of melting point and the bond strength of the elements present in the alloys.

3.11.2 Thermal stability

The sequence of phase evolution of the non-equiatomic high entropy steel at different temperatures is illustrated as follows: 25 ℃, the phase forms are BCC + γ-brass type + B2-type + Si (undissolved). At 420 ℃, the phases are BCC + γ-brass type + B2-type. However, the phase fraction of the γ-brass type structure was increased, and ordering or texturing of the phases happened. This type of transformation was also evident in $Fe_{40}Cr_{25}Ni_{15}Al_{15}Co_5$ medium entropy alloy [148] and quasicrystals [243]. The alloy is thermally stable up to ~500 ℃, afterwards, at 520 ℃, the phases present are BCC + γ-brass type + B2-type and Fe_5Si_3 type silicide. The gamma-brass (secondary phase) is formed after the mechanical alloying as metastable phase, which shows

the texturing in between 400 ℃ to 500 ℃, but in small amount (around 4 %). After 600 ℃ it dissolves, and transformed into more stable phases. It was observed in the conventional steels and Fe-based HEAs, that this type of brass-type structure (also known as χ-type) is formed, but this is generally metastable, and after certain temperature region they transformed in to more stable phases at higher temperature [244, 245]. This silicide formation was also observed at higher temperatures of non-equiatomic AlCoCrFeNiSi [246] and AlCrFeMgNi [247] HEAs fabricated using the powder metallurgy route. The phase transformations that occurred at higher temperatures were due to the formation of the metastable solid solution phase during the milling. For $Fe_{36}Mn_{21}Cr_{18}Ni_{15}Al_{10}$ high entropy alloy, the phases formed were BCC and B2. The alloy showed the thermal stability of the B2 phase at different heat treatments of the as-cast samples. The good thermal stability of the B2 phase was due to the strong bonding between the Ni-Al atoms and the sluggish diffusion effect in the HEAs [148, 149]. In the present alloy, the retention of the BCC and B2 phase after the various annealing conditions and SPSed was due to the strong bonding between the pairs of Fe-Al and Ni-Al, and the sluggish diffusion effect. The formation of the silicide was due to the undissolved Si remaining after milling, and it has the tendency to form the silicide with Fe and Mn, as the binary enthalpy of mixing between Fe-Si and Mn-Si is highly negative.

Further, the sequence of the phase evolution after milling, annealing, and SPS are correlated with the CALPHAD predicted phases, which is illustrated in Figure 3.18(a). The property diagram of the non-equiatomic high entropy steel is generated using the ThermoCalc software. The sequence of the predicted phase is as follows:

- The liquid (100%) forms at around 1200℃ which contains all the elements of the alloy system i.e., Fe, Mn, Ni, Al, Si, and C.

- Around 1100 ℃, from the liquid, the two phases formed i.e., BCC_A2#1 phase (which contains Fe, Mn, Ni, Al, Si, and C), and B2 (contains Ni and Al), as illustrated in Figure 3.18(b and c), respectively. This prediction was very well correlated with the phase formed after the spark plasma sintering.

- Around 800 ℃, the number of phases formed remained the same, and afterwards, the BCC_A2#2 phase was formed (contains Mn and C), as shown in Figure 3.18(d).

- In between 800 ℃ and 500 ℃, the M_5Si_3 intermetallic compound was formed, which is enriched in Fe, Mn, and Si, as displayed in Figure 3.18(e). This type of phase evolution was also evident in a 600 ℃ annealed sample.

- Around 300 ℃, the BCC_A2#1, B2, BCC_A2#2, and M_5Si_3 are retained and the new phase is evolving BCC_A2#3 which is enriched in Fe, Mn, and Si, which is shown in Figure 3.18(f). After this, the phases remain unaltered up to room temperature.

However, some key dissimilarities between the two results are observed: BCC_A2#2 containing only Mn and C predicted as a separate phase, but this kind of phase is not seen in the experimental result. CALPHAD predictions showed the B2 type as the pure binary of Al and Ni, but in experimental findings, it is enriched in Fe, Ni, and Al. Partial melting of the high entropy steel started around 870 ℃, but this type of partial melting was not observed in the DSC analysis up to 1000 ℃. This reflects that the phase prediction of the HEAs is challenging, as HEAs have a vast compositional space that has to be investigated with relatively less data as compared to conventional alloys. Therefore, the differences in the predicted and the experimental results were due to the limitations of the CALPHAD database.

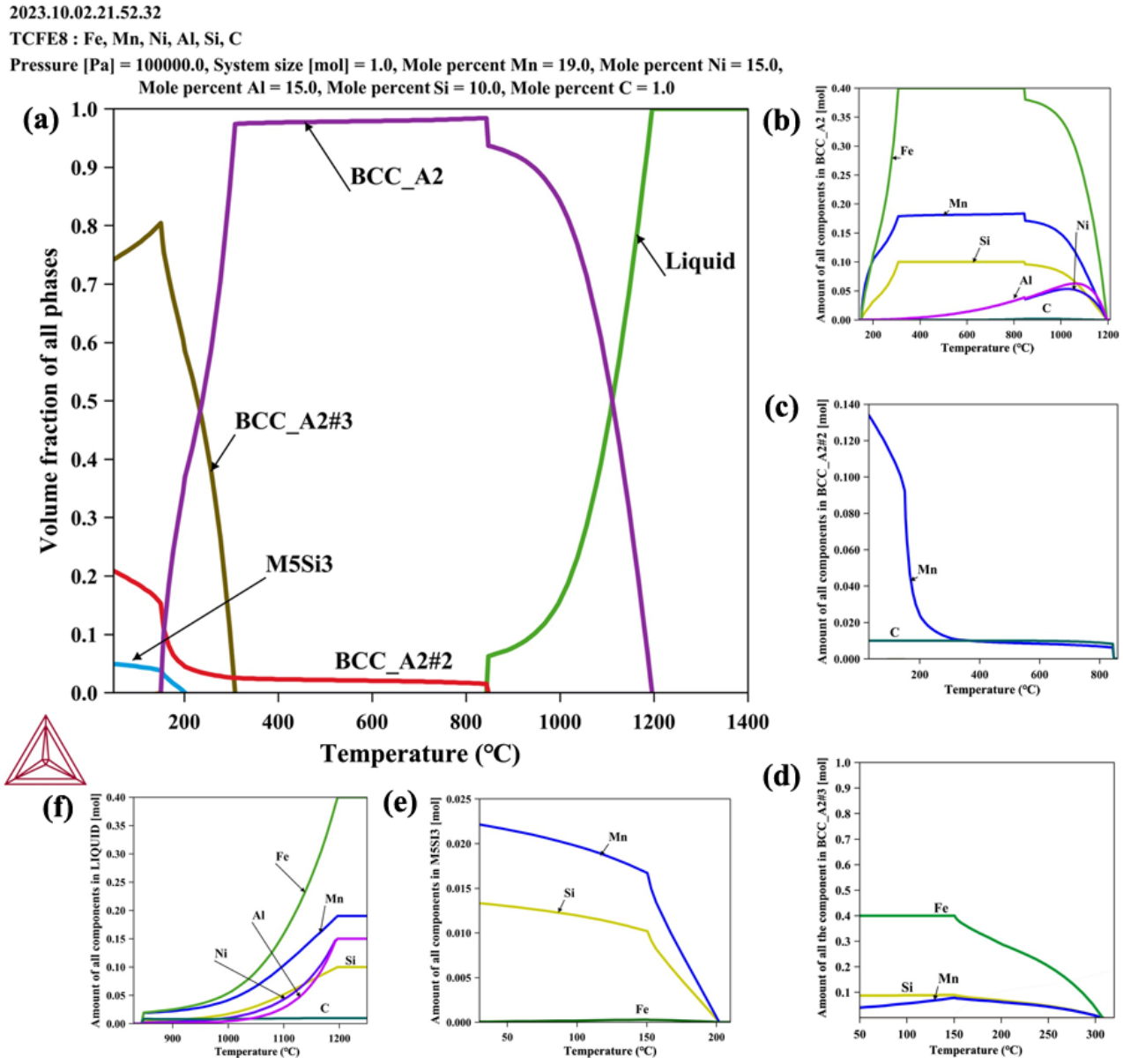

Figure 3.18: Property diagram represent the phase transformation and phase composition with the function of temperature through CALPHAD modelling (TCFE8) in the non-equiatomic FeMnNiAlSiC high entropy steel. (a) Amount of all the phases versus temperature; (b-f) The elemental composition in all the phases and their stability with respect to temperature.

3.11.3 Mechanical properties and strengthening mechanism

The measured compressive yield strength of the high entropy steel was found to be 2000 ± 200 MPa, this is the combination of frictional stress and the various strengthening mechanisms

including grain boundary, precipitates, dislocation, and solid solution strengthening. The total yield stress can be calculated from equation no. 1.9, the terms used in equations are σ_o is frictional stress, σ_{gb} is grain boundary strengthening, σ_p is precipitates strengthening, σ_d is dislocation strengthening and σ_{ss} is solid solution strengthening. The frictional stress was taken as 120 MPa for BCC and B2-type [225]. The grain boundary strengthening was calculated using the Hall-Petch relation, which is given in equation no. 1.13, the term K_o is the constant related to the material, and the value was taken as 574 MPa/$\mu m^{1/2}$ for BCC and partially ordered B2-type [248], respectively and the value of the grain size (d) (it is calculated using the ImageJ software from the SEM image, shown in Figure 3.10 (b)) for BCC and B2-type was found to be 0.28 μm and 0.22 μm, respectively. The value for grain boundary strengthening was evaluated to be 1085 MPa and 1224 MPa for BCC and B2-type, respectively.

The effect of the silicide and the B2-type precipitate on the strength of the high entropy steel was calculated using the Orowan mechanism for precipitate strengthening, which is calculated using equation no. 1.14, in which termed used are, M is the Taylor factor (2.73) [249], G is the shear modulus, calculated using the rule of mixture and its value is found to be 75.34 GPa, υ is the Poisson's ratio (0.3), b is the Burger vector, and its calculation detail is given in subsection 2.3.1, λ is the spacing between the precipitates and calculated using the equation no. 1.15, where f is the volume fraction of the precipitates (8.4 % for Fe_5Si_3-type and 34 % for B2-type), $\bar{r}$ is the average radius (circular cross-section) of the spherical precipitates, and details are given in subsection 1.10, in which the termed used are r is the average radius of the precipitates (102 nm for Fe_5Si_3-type and 220 nm for B2-type). The value of the dispersion strengthening for the BCC phase was found to be 54 MPa and 111 MPa for silicide and B2-type, respectively, and for the B2-type phase was found to be 55 MPa for silicides.

The contribution of the dislocation strengthening was calculated using the Bailey-Hirsch relationship and can be taken from equation 1.12, and the values of the various terms in the equations are, $\alpha = 0.2$ for BCC and B2-type [248], respectively, b is the Burger vector and ρ_{dd} = dislocation density, which is calculated using the equation 2.2, where, t is crystallite size in nm, b is Burger's vector and its calculation detail is given in subsection 2.3.1, and ε = microstrain, and its value is mentioned in Table 3.3. The microstrain was calculated using equation 2.3, where, θ = Bragg angle, and β = FWHM, and the value was taken as 4.46×10^{15} m^{-2} and 3.36×10^{15} m^{-2}, for BCC and B2-type, respectively. The value was found to be 687 MPa and 590 MPa for BCC and B2-type respectively.

The concept of the solute and solvent is obsolete for HEAs, so solid solution strengthening calculations are different from the conventional approach. However, the atomic radii of Fe and Ni are similar and Si has less atomic radius as compared to Fe. The binary enthalpy of the Fe-Mn pair is nearly zero, and the atomic radius of Al is 15 % higher than the Fe, Ni, and Si, that's why FeMnNiSi is taken as the solvent matrix and Al as the solute element. So, the standard Fleischer model is taken for the calculation of solid solution strengthening, which is given in equation no. 1.10. The Al was taken as the solute element for both, the BCC and B2-type phases, and its value is taken as 13.45 and 36.55, respectively. The value was found to be 106 MPa and 177 MPa for BCC and B2-type, respectively.

The strengthening mechanism calculation was done on the assumption that the phase fraction of the BCC and B2-type was 100%. The phase fraction of BCC and B2-type in the SPSed sample of the high entropy steel was calculated as 56.0 % and 34.0 %, respectively. Therefore, the phase fraction of the BCC and B2-type for the calculation of the strengthening mechanism was taken as 62.0 % and 38.0 %, respectively. The contribution of the various strengthening mechanisms is

shown in the bar chart in Figure 3.19 (a). The grain boundary and dislocation strengthening are the dominant strengthening mechanisms. The individual contribution of different strengthening mechanisms is displayed in Figure 3.19 (b). Some discrepancy was observed in the calculated and measured strength due to the following reasons, firstly the parameters taken are approximated and cited from other HEAs [248].

It was observed that the addition of the Si element promotes the formation of the BCC phase and silicide with Cr, Fe, Ni, and Ti elements in the HEAs [249]. It was reported that the mechanical properties i.e., hardness and strength increased with the addition of the Si element in the HEAs [250]. $Al_{0.3}CoCrFeNiSi_x$ showed the phase transformation from FCC to BCC/ordered B2 phase as x increases (x = 0 to 1 at. %). The tensile strength and hardness of the HEAs increased without any decrease in the tensile ductility by 63 %, and 143 HV to 863 HV as Si increased from (x = 0-1 at. %) [250]. Wang et al. [251] reported that the formation of M_5Si_3 type silicide in the HEAs, which enhanced the strength and plasticity. The strength and plasticity both increased with the small content of the Si element, but as Si increases, the strength increases but plasticity decreases in the HEAs [251]. In $Al_{0.2}Co_{1.5}CrFeNi_{1.5}Ti_{0.5}$ HEA, the silicide formation played a crucial role in strengthen the alloy, as it increased the hardness and compressive strength of the alloys [177]. In contrast to previous work on high entropy steel and HEAs, the present alloy has shown a high hardness, and its value is 7.8 GPa. $Fe_{36}Mn_{21}Cr_{18}Ni_{15}Al_{10}$ HEAs showed room temperature ductility greater than 30 %, and the phases formed are dual-phase structures of BCC + B2, which stated that due to the cocktail effect such high ductility in the HEAs system is achieved [149]. In the present alloy, the in-situ formation of the silicide has played a crucial role in strengthening the alloy i.e., microhardness and compressive strength with a good amount of ductility.

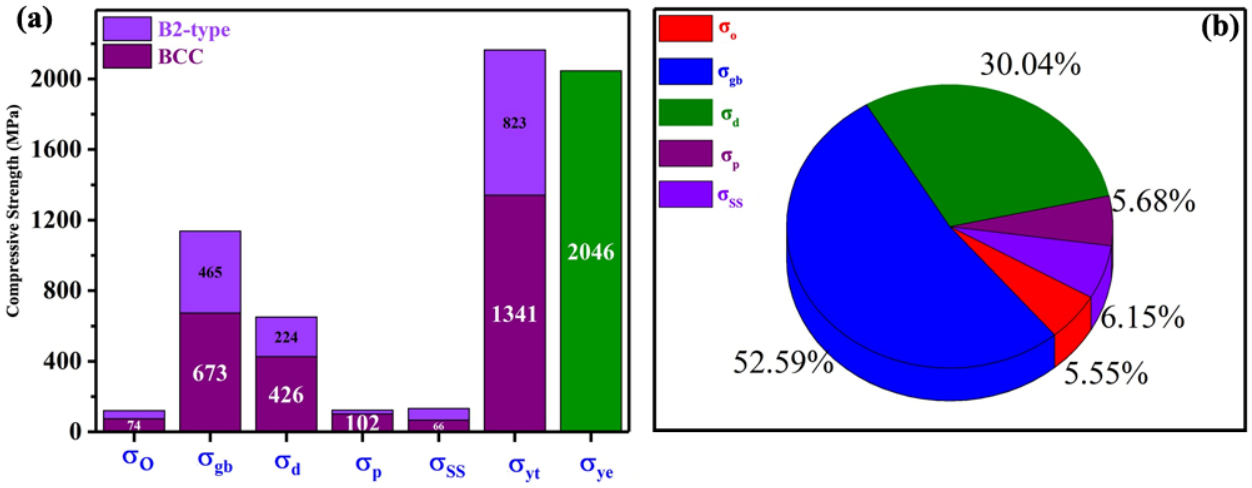

Figure 3.19: (a) The values of the various strengthening mechanism and experimental yield strength (Bar plot); (b) The pie chart for the percentage's contribution of the various strengthening mechanism.

The ferritic dual-phase steel has microhardness values in the range of 2.0-2.4 GPa [169]. The microhardness of the present alloy is three times to hardness of the dual-phase steel. The microhardness comparison of the present alloy with respect to reported HEAs is listed in Table 1.3. The low-density high entropy steel with the formation of BCC and B2 coexisting with silicide showed excellent mechanical properties i.e., compressive strength and microhardness as compared with the HEAs and conventional steel. The present investigation envisaged fabricating a low-density high entropy steel possessing good microstructural stability as well as excellent mechanical properties having synergy with ductility. In spite of having excellent microstructural stability and mechanical properties, these SPSed HES were found to have a good ductility of ~19%.

3.11.4 Wear behaviour and biocompatibility

The variation in the CoF curve with time is due to the following reason: during the friction and wear process, the wear debris is constantly being produced and lie on the wear track, making it irregular and serrated. So, this frictional contact between ball and surface never comes to the state

of relative dynamic balance, which results in fluctuations in CoF curves. Further, the wear debris is stuck in the surface, which leads to the development of local cracks in the wear track which is also responsible for the fluctuation in CoF [236]. The low specific wear rate of the high entropy steel was due to the formation of the dual-phase structure i.e., BCC and B2 with the Fe_5Si_3 type silicide precipitates. The alloys have high hardness with an appreciable amount of ductility. The wear resistance of FeMnNiAlSiC high entropy steel is better than conventional 316L steel and many reported HEAs [252–255].

Better biocompatibility of the present alloy system than 316L is due to the presence of Si in combination with Fe; it forms silica–iron, which exhibits good biocompatibility in MG-63 cell and there is no cytotoxicity [256]. Porous silicon has already been used for chronic eye disease and bone regeneration [257–259]. Moreover, the alloying effect of Si in (Ti–Zr–Pd–Si–(Nb), Fe-Mn, and Mg–Si alloys have shown better cell viability, proliferation, and biocompatibility [260–262].

3.12 Conclusions

The phase evolution of the $Fe_{40}Mn_{19}Ni_{15}Al_{15}Si_{10}C_1$ high entropy steel after high energy ball milling, and their thermal, structural, and microstructural stability after spark plasma sintering were evaluated. Further, experiments were done to determine the mechanical properties i.e., microhardness, elastic modulus, and compressive strength of the SPSed sample, and the surface properties i.e., tribology studies at dry condition and biocompatibility. The following conclusions can be drawn from the present study:

1. After 35 h of mechanical milling the phases formed were BCC, partially ordered B2-type and γ-brass type structure. The metastable alloy showed thermal stability up to 500 ℃. Afterward, the Fe_5Si_3-type intermetallic phases were formed at 520 ℃. The formation of

silicide at higher temperatures could be due to higher binary enthalpy between the Fe-Si and atomic size mismatch.

2. The BCC and B2-type phases were retained after spark plasma sintering along with the formation of the Fe_5Si_3-type silicide phase. The nanocrystalline structure was observed after annealing treatment and spark plasma sintering of the powdered samples.

3. The dual-phase structure i.e., BCC and B2 showed good strength i.e., microhardness (7.8 ± 0.3 GPa) and yield compressive strength (2000 ± 200 MPa) with a good amount of compressive ductility (19 %). The calculated values of strengthening based on materials modelling were close to the experimental values. The grain boundary and dislocation strengthening are found to be the dominant mechanisms. The phase prediction through thermodynamic parameters and ThermoCalc were correlated with the experimental results.

4. This high entropy steel showed good wear resistance against the hard ceramic counter ball (Al_2O_3), and the values of the specific wear rate were found to be 1.79 – 4.36 x 10^{-5} mm^3/mN. The dominant wear mechanism of high entropy steel is abrasive wear. This alloy showed good biocompatibility in the MG-63 cell as compared with the control (316L). So, this alloy can also be used for biomaterial applications.